# Chapter 2
# Preliminaries of 3D Point Cloud Processing

In this chapter, we provide preliminaries of 3D point cloud processing. For this purpose, we first describe the general concept of scene acquisition (Sect. 2.1) and subsequently provide basic definitions for the most important terms which are important to consider the contents presented in this book in the global context (Sect. 2.2). Based on these explanations, we focus on the use of 3D point cloud data and explain how 3D point cloud data may be acquired (Sect. 2.3) and how 3D point cloud data may be transformed to respective 2D image representations in the form of range images and intensity images (Sect. 2.4). Since acquired 3D point cloud data is typically corrupted with a certain amount of noise, we enlighten the issue of filtering raw 3D point cloud data in terms of removing unreliable 3D points (Sect. 2.5). In this regard, we present two novel measures for point quality assessment and discuss their chances and limitations in detail. Finally, we provide concluding remarks (Sect. 2.6).

## 2.1 From the Real World to a Scene and Its Representation

In order to transfer specific capabilities of human visual perception to fully automated systems, the main goal consists of gathering information about the *real world* for which we may generally involve different sensor types. However, similar to human vision, the sensor types typically reveal a limited field-of-view and partially also a limited perception in case of distant objects. Thus, it is impossible to describe the real world as a whole but only a small part, and we will therefore define a *scene* as the considered part of the real world, i.e., a collection of shapes and reflectance [39].

Considering a scene with a specific sensor type (Fig. 2.1), the sensor type establishes a function for mapping the considered scene onto *data*. In this regard, the use of different sensor types (e.g., digital cameras, thermal cameras, multispectral cameras, range cameras, laser scanners, etc.) typically results in data in the form of 2D imagery or 3D point cloud data. In the context of decision and control tasks, however, the measured data generally has no information since it is only measured data, whereas *information* reduces the uncertainty with respect to a specific *task* or



M. Weinmann, *Reconstruction and Analysis of 3D Scenes*,
DOI 10.1007/978-3-319-29246-5_2

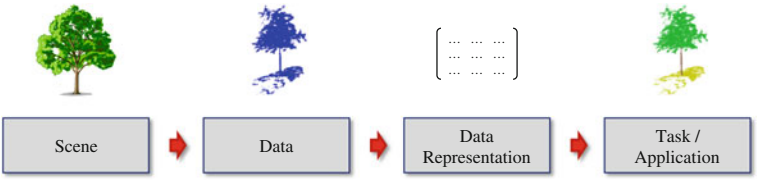


**Fig. 2.1** Generalized relation between scene, data, data representations, and task: the scene (e.g., a tree) is mapped onto data (e.g., 3D point cloud data) which, in turn, is transformed into a different data representation (e.g., specific features) suited to solve a specific task (e.g., 3D scene analysis)

an *application*. In the following chapters, we will assume that the measured data contains information which might help us to reduce the uncertainty about a specific task, e.g., to estimate the viewpoint or to recognize objects.

The acquired data in the form of 2D imagery or 3D point cloud data is however typically not suited for solving specific tasks directly and, consequently, the data has to be transferred to a different *data representation* being a specific description and thus a function of the data. This means that a transformation of data from one space to another encoding is involved, whereby the transformation is described via a *function* which, in turn, may be based on a model, some lines of code or an algorithm, and typically depends on the respective task. For instance, it may be desirable to try to take away as much as possible from the data and retain as much as matters for the task, i.e., to preserve only the information which is relevant for a specific task. Note that this is in accordance with the idea to keep all the data if we do not know the task. Furthermore, we may extend these considerations by introducing a *memory* as a mechanism to store data or data representations and *knowledge* as something useful one may draw conclusions from.

Note that the applied definition of *information* follows seminal work [39, 40] which is in contrast to traditional information theory based on fundamental ideas of Claude Elwood Shannon and Norbert Wiener. Traditional information theory considers information as "complexity of the data, regardless of its use and regardless of the nuisance factors affecting it," whereby the complexity of the data is often described with the entropy of a respective distribution and nuisance factors may for instance be represented by contrast, viewpoint, illumination, occlusions, quantization, and noise [40]. With increasing complexity of the data, it becomes more and more costly to store and transmit the data. Thus, the traditional definition of information is tailored to data storage/compression and transmission tasks, where the semantic aspect of the data is irrelevant[1] [40]. However, if we intend to use the data for a different task, a different definition may be desirable which—as for instance stated in [39]—also accounts for questions regarding the information an image contains about the scene it portrays or the value of an image for recognizing objects in the scene or navigating through the scene. Consequently, the definition of information should rather

[1] Note that, in the context of data storage/compression and transmission tasks, the most costly signal is represented by white noise [40].

address the part of the data that matters for the task and thus be defined relative to the scene. This, in turn, is in accordance with biological systems that perceive stimuli and perform actions or make decisions in a way that maximizes some decision or control objective [40], e.g., in order to intelligently interact with the surrounding. For this reason, we follow the ideas presented in [39, 40] and consider the notion of information in the context of performing a decision or action based on sensory data, whereby a decision may represent any task of detection, localization, categorization, and recognition of objects [40]. By focusing on the definition of information as the part of the data that matters for the task, the complexity of the data is not relevant to decision and control tasks[2] [40]. For more detailed and further considerations, we refer to [40].

## 2.2 On Points and Clouds, and Point Clouds

In this section, we intend to provide basic definitions for the most important terms used across the whole book:

- The term *point* is used as in geometry, where it specifies a unique location in a specific space. In the scope of our work, we consider the Euclidean space $\mathbb{R}^D$ with $D = 2$ for points in 2D imagery such as image locations or 2D keypoints and $D = 3$ for points in 3D space such as scanned 3D points, reconstructed 3D points, or 3D keypoints. Hence, a point has no dimensions such as length, area, or volume.
- While there is certainly a meteorological association, we refer the term *cloud* to cloud computing and thus a complex interplay of application systems which are executed externally (within the cloud) and operated via specific interfaces (mostly via internet platforms). In this regard, different applications focus on (i) the external processing of computationally intensive methods in terms of runtime and memory and (ii) the transfer of results to smartphones, tablets, notebooks, desktop computers, or servers, e.g., in the form of web services.
- The term *point cloud* is used to describe a set of data points in a given space. Following [32], we may consider a point cloud as a data structure used to represent a collection of multidimensional points. As our focus is clearly set on 3D point clouds representing the measured or generated counterpart of physical surfaces in a scene, we will concentrate on 3D point clouds as a collection of 3D points which, in turn, are characterized by spatial *XYZ*-coordinates and may optionally be assigned additional attributes such as intensity information, thermal information, specific properties (e.g., in terms of orientation and scale), or any abstract information.

Even though it is intended that some of the developed concepts and methods are integrated in a web service, we only focus on data processing on notebooks, desktop computers, or servers without cloud computing. This is in analogy to a variety of

[2] Note that extremely complex data may be useless for a decision, while extremely simple data could directly be relevant for the same decision [40].

research domains where the development of efficient methods with respect to processing time, memory consumption, and financial costs is in the focus. For instance, the 3D reconstruction of large parts of the city of Rome, Italy, has been conducted based on 150 k images in less than a day on a huge cluster with almost 500 cores [1]—which we may refer to as a data processing on a *cloudy day* due to the involved cloud computing—whereas the processing of large photo collections within the span of a day on a single PC may be referred to as a processing on a *cloudless day* [13] which is certainly favorable considering the related financial costs.

## 2.3 Point Cloud Acquisition

As all the concepts and methods developed in the scope of our work are based on the use of 3D point cloud data as input, we will briefly discuss the acquisition of such 3D point cloud data. Generally, the acquisition of 3D point clouds representing the counterpart of physical object surfaces in a scene has been widely investigated over the last decades. While a variety of acquisition systems based on different principles may be involved, particularly the optical methods have proven to be favorable as they offer an efficient, touchless, and even far-range acquisition of 3D structures in both indoor and outdoor environments—from small scales such as single rooms up to large scales such as city scale or even beyond—and, thus, they have gained much importance in photogrammetry, remote sensing, computer vision, and robotics.

Generally, we may categorize the different techniques proposed for optical 3D shape acquisition with respect to the measurement principle they are based on, and numerous valuable surveys following this categorization may be found in literature [10, 20, 30, 34, 57]. Basically, this categorization first focuses on the distinction between passive and active techniques. While *passive techniques* are used for scenes with reasonable ambient lighting conditions and only collect information, *active techniques* focus on actively manipulating the observed scene, e.g., by projecting structured light patterns in the form of stripe patterns or point patterns via emitting electromagnetic radiation in either the visible spectrum or in the form of laser light (typically in the infrared (IR) spectrum). Based on this more general distinction, a further distinction may directly refer to the spatial arrangement of viewpoints and the positions of involved illumination sources. In this regard, passive techniques may be based on a single view or on multiple views of a scene. For active techniques, one may furthermore distinguish between a monostatic sensor configuration, where the emitter component and the receiver component are at the same location, or a multistatic configuration, where the emitter component and the receiver component are spatially separated and even several of such components may be involved. From these distinctions, a taxonomy of optical 3D shape acquisition techniques as illustrated in Fig. 2.2 may be derived. In order to understand the main principles and the basis for the subsequent chapters, we provide a short description of the most important ideas in the following subsections. For an exhaustive survey, we refer to the aforementioned literature. However, we want to point out that, depending on the

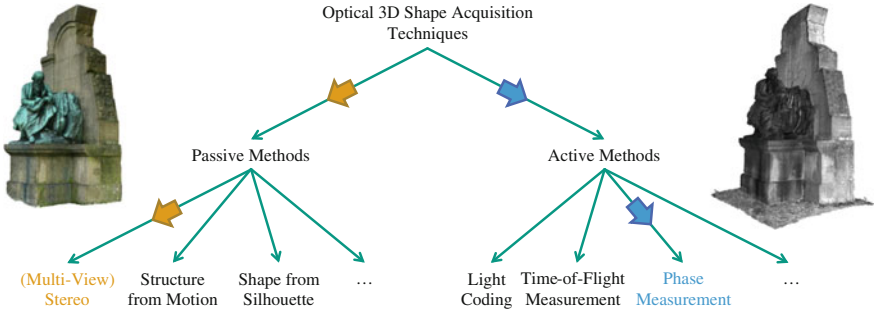


**Fig. 2.2** Taxonomy of optical 3D shape acquisition techniques, an exemplary point cloud derived via Multi-View Stereo (MVS) techniques (*left*) and an exemplary point cloud derived via phase-based measurements (*right*)

involved acquisition technique and the used device, the acquired 3D point cloud data may be corrupted with more or less noise and, in addition to spatial 3D information in the form of $XYZ$-coordinates, respective point attributes such as color or intensity information may be acquired as well. Furthermore, it should be taken into account that—despite a variety of optical 3D shape acquisition techniques—shape reconstruction still remains challenging for surfaces which exhibit a complex surface reflectance behavior such as highly specular object surfaces as given for mirroring objects where an adequate 3D reconstruction may, for instance, be achieved via more sophisticated techniques [56].

### *2.3.1 Passive Techniques*

Passive techniques for point cloud generation only rely on radiometric information represented in the form of 2D imagery and thus simple intensity measurements per pixel. In order to reconstruct 3D structures from such intensity images, different approaches have been presented and we will focus on the two most commonly applied strategies.

The first strategy is followed by *stereo matching techniques* which exploit two or more images of a scene, acquired with either multiple cameras or one moving camera, and estimate the respective 3D structure of the scene by finding corresponding points in the intensity images and converting their 2D locations into 3D depth values based on triangulation [36, 46]. Classical stereo matching techniques are based on the use of two images due to early findings in human visual perception according to which the depth of a scene is perceived based on the differences in appearance between what is seen by the left eye and the right eye. In contrast, Multi-View Stereo (MVS) techniques focus on reconstructing a complete 3D object model from a collection of images taken from known viewpoints [37].

The second strategy is followed by *Structure-from-Motion* (*SfM*) *techniques* which focus on the simultaneous recovery of both the 3D structure of a scene and the camera pose from a large number of point tracks, i.e., corresponding image locations [46]. One of the most general approaches to SfM has been presented with *Bundle Adjustment* [47] which is able to simultaneously recover 3D structures, camera pose, and even the intrinsic camera parameters via the consideration of bundles of rays connecting the camera centers to 3D scene points and an adjustment in terms of iteratively minimizing the reprojection error.

### *2.3.2 Active Techniques*

Whereas passive techniques only rely on information arising from simple intensity measurements per pixel, active techniques are based on actively manipulating the observed scene by involving a scanning device which emits a signal and records information arising from respective observations in the scene. In this context, the emitted signal may either be a coded structured light pattern in the visible or infrared spectrum, or electromagnetic radiation in the form of modulated laser light. For both cases, we briefly reflect the basic ideas in order to understand the measurement principles of the scanning devices used in the following chapters.

Scanning devices exploiting *structured light projection* actively manipulate the observed scene by projecting a coded structured light pattern, and thus manipulating the illumination of the scene. Via the projected pattern, particular labels are assigned to 3D scene points which, in turn, may easily be decoded in images when imaging the scene and the projected pattern with a camera. Accordingly, such synthetically generated features allow to robustly establish feature correspondences, and the respective 3D coordinates may easily and reliably be recovered by triangulation. Generally, techniques based on the use of structured light patterns may be classified depending on the pattern codification strategy [10, 33]:

- Direct codification strategies exploit a pattern which is typically based on a large range of either gray or color values. Thus, each pixel may be labeled with the respective gray or color value of the pattern at this pixel.
- Time-multiplexing strategies exploit a temporal coding, where a sequence of structured light patterns is projected onto the scene. Thus, each pixel may be assigned a codeword consisting of its illumination value across the projected patterns. The respective patterns may, for instance, be based on binary codes or Gray codes and phase shifting.
- Spatial neighborhood codification strategies exploit a unique pattern. The label associated to a pixel is derived from the spatial pattern distribution within its local neighborhood. Thus, labels of neighboring pixels share information and provide an interdependent coding.

Representing one of the most popular devices based on structured light projection, the Microsoft Kinect exploits an RGB camera, an IR camera, and an IR projector.

The IR projector projects a known structured light pattern in the form of a random dot pattern onto the scene. As IR camera and IR projector form a stereo pair, the pattern matching in the IR image results in a raw disparity image which, in turn, is read out in the form of an 11-bit depth image. For respective investigations on the accuracy and capabilities of Microsoft Kinect, we refer to [25, 38, 53, 59].

A different strategy for measuring the distance between a scanning device and object surfaces in the local environment is followed by exploiting *Time-of-Flight* (*ToF*) *or phase measurements* which are typically exploited by terrestrial or mobile laser scanners and by Time-of-Flight (ToF) cameras. According to seminal work [21, 24, 44], respective scanning devices may be categorized with respect to laser type, modulation technique, measurement principle, detection technique, or configuration between emitting and receiving component of the device. Generally, such scanning devices illuminate a scene with modulated laser light and analyze the backscattered signal. More specifically, laser light is emitted by the scanning device and transmitted to an object. At the object surface, the laser light is partially reflected and, finally, a certain amount of the laser light reaches the receiver unit of the scanning device. The measurement principle is therefore of great importance as it may be based on different signal properties such as amplitude, frequency, polarization, time, or phase. Many scanning devices are based on measuring the time $t$ between emitting and receiving a laser pulse, i.e., the respective *time-of-flight*, and exploiting the measured time $t$ in order to derive the distance $r$ between the scanning device and the respective 3D scene point. Alternatively, a range measurement $r$ may be derived from phase information by exploiting the phase difference $\Delta\phi$ between emitted and received signal. However, the phase difference $\Delta\phi$ only is a wrapped phase and thus the corresponding range is ambiguous so that multiples of $2\pi$ have to be added in order to recover the unwrapped phase $\phi$ and an appropriate range measurement $r$. For such a disambiguation, various image-based or hardware-based phase unwrapping procedures have been proposed [12, 22, 23]. In order to get from single 3D scene points to the geometry of object surfaces, respective scanning devices are typically mounted on a rotating platform[3] which, in turn, allows a sequential scanning of the scene by successively measuring distances for discrete points on a given scan raster. Due to the sequential scanning, however, respective scanning devices are not suited for the acquisition of dynamic scenes. In contrast, modern range cameras use a sensor array which allows to simultaneously acquire range information for all points on the considered scan raster and thus estimate the scene geometry in a single shot. Such range cameras meanwhile allow to acquire depth maps at relatively high frame rates of about 25 fps [10, 26, 31, 57] and are thus also applicable in order to capture dynamic scenes.

[3] In this context, a rotation around a single rotation axis is for instance applied for line laser scanners which thus provide measurements on a 1D scan grid, whereas standard terrestrial laser scanners involve a rotation in both horizontal and vertical direction in order to provide measurements on a 2D scan grid.

## 2.4 Generation of 2D Image Representations for 3D Point Clouds

In the scope of our work, we focus on point clouds acquired with (terrestrial or mobile) laser scanners and range cameras. Thereby, laser scanners typically capture data by successively considering points on a discrete, regular (typically spherical) raster, and recording the respective geometric and radiometric information. In contrast, range cameras have an internal sensor array for simultaneously considering all points on a discrete, regular (typically planar) raster, and recording the respective geometric and radiometric information. If the data acquisition is performed sufficiently fast, range cameras also allow an acquisition of dynamic scenes. For both types of acquisition systems, however, the sampling of data on a discrete, regular raster allows to derive 2D image representations for spatial 3D information and the respective radiometric information. While the spatial 3D information and thus its 2D representation in the form of a range image, where each pixel represents the distance $r$ between the scanning device and the respective 3D scene point, depend on the scene structure, the captured radiometric information depends on both the scene structure and the signal processing unit in the involved acquisition system. Note that differences with respect to the signal processing unit mainly arise from internal processes such as the conversion to a digital signal and signal amplification which are not identical for different scanning devices.

In order to derive a representation which is independent of the involved scanning device, it is feasible to transform the radiometric information representing the measured energy of the backscattered laser light from arbitrary values to a given interval of possible values. In this context, the radiometric information represented in a matrix $\mathbf{I} \in \mathbb{R}^{n \times m}$ with $n$ rows and $m$ columns is typically transformed to an 8-bit gray-valued image $\mathbf{I}_{\text{norm}}$ by performing a histogram normalization of the type

$$\mathbf{I}_{\text{norm}} = \text{uint8}\left(255 \cdot \frac{\mathbf{I} - I_{\min} \cdot \mathbf{1}_{n \times m}}{I_{\max} - I_{\min}}\right) \tag{2.1}$$

where $I_{\min}, I_{\max} \in \mathbb{R}$ are the minimum and maximum values of $\mathbf{I}$, respectively. Thus, the elements of the resulting $(n \times m)$-matrix $\mathbf{I}_{\text{norm}}$ are represented by integer values in the interval $[0, 255]$.

Considering the adapted radiometric information, we may describe a scan $\mathscr{S} = \{\mathscr{I}_{\text{R}}, \mathscr{I}_{\text{I}}\}$ with respective 2D representations in the form of a range image $\mathscr{I}_{\text{R}} \in \mathbb{R}^{n \times m}$ and an intensity image $\mathscr{I}_{\text{I}} = \mathbf{I}_{\text{norm}} \in \mathbb{R}^{n \times m}$. On both types of images, we may apply standard image processing techniques, e.g., to detect specific features or to recognize and segment objects. In order to obtain an impression about the characteristics of such images, we consider a scan taken from a benchmark dataset[4] [9] which is later

[4] This dataset is available at http://www.ikg.uni-hannover.de/index.php?id=413\&L=de (last access: 30 May 2015).

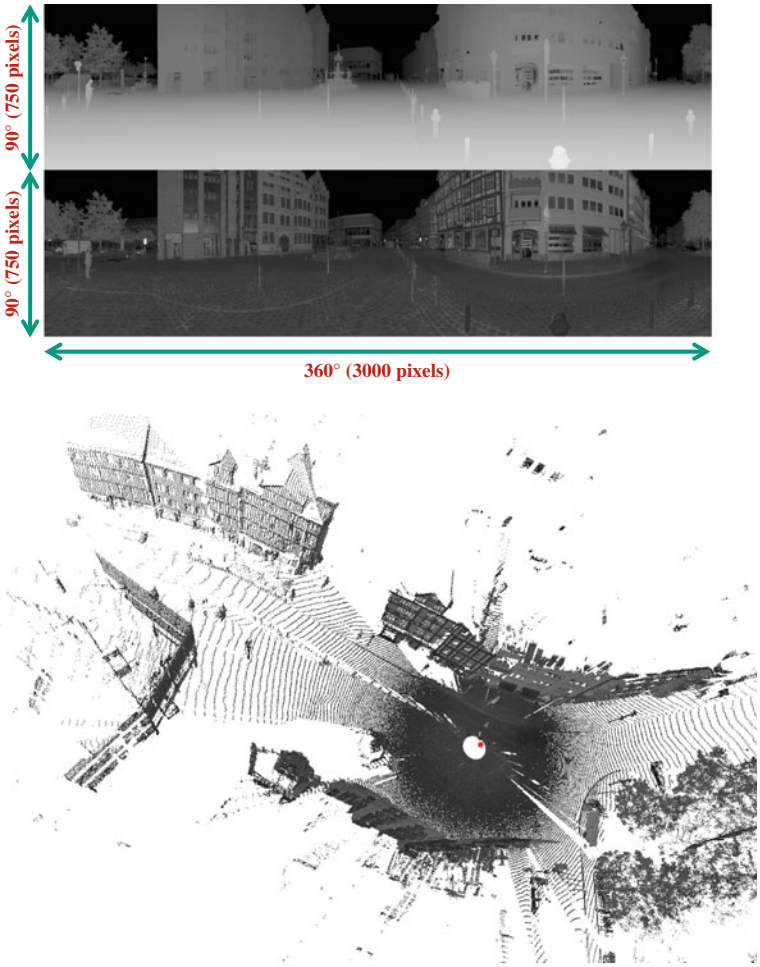


**Fig. 2.3** Range image $\mathscr{I}_R$ and intensity image $\mathscr{I}_I$ (*top*), and a visualization of the scan as 3D point cloud where the position of the scanning device is indicated by a *red dot* (*bottom*)

used for evaluating novel approaches for point cloud registration in Chap. 4. The respective range image $\mathscr{I}_R$ as well as the respective intensity image $\mathscr{I}_I$ are shown in Fig. 2.3.

## 2.5 Point Quality Assessment

When dealing with 3D point cloud data, it should be taken into account that, usually, a filtering of the raw point cloud data is carried out by internal software provided by the manufacturer of a device. Thus, the applied methodology is hidden in a

"black box" whose procedures may hardly be reconstructed. Consequently, we aim to found our methodology on raw 3D point cloud data and, hence, understand the routines applied for filtering 3D point cloud data by removing unreliable range measurements. In order to do so, we first reflect different factors which influence the quality of a range measurement as well as existing approaches for quantifying the quality of a range measurement (Sect. 2.5.1). Based on these considerations, we proceed with describing a standard approach based on intensity information (Sect. 2.5.2) and, subsequently, we present two novel approaches based on *range reliability* (Sect. 2.5.3) and *local planarity* (Sect. 2.5.4) which have been developed in the scope of our work. In order to reason about their suitability, we provide a qualitative comparison (Sect. 2.5.5) as well as a quantitative comparison (Sect. 2.5.6) of these approaches.

### *2.5.1 Influencing Factors and Related Work*

Generally, the quality of a range measurement depends on a variety of influencing factors. Following seminal work on categorizing these factors [6, 18, 19, 43], we take into account four different categories:

- The first category of influencing factors is based on the design of the acquisition system which, according to [21, 44], may be characterized by the laser type, the modulation technique (e.g., continuous wave or pulsed lasers), the measurement principle (e.g., time-of-flight, phase or amplitude measurements), the detection technique (e.g., coherent or direct detection), and the configuration between transmitting and receiving unit (e.g., monostatic or bistatic configuration). Concerning these components, specific factors influencing individual point quality mainly arise from respective hardware properties (e.g., angular resolution, angular accuracy, and range accuracy) and the calibration of the used device (e.g., calibration model or short-term/long-term stability).
- The second category of influencing factors addresses atmospheric and environmental conditions [7, 49]. While uncertainties due to atmospheric conditions mainly arise from humidity, temperature, aerosols (i.e., fine solid particles or liquid droplets in the air), or variations in air pressure, the environmental conditions address the presence of ambient lighting (i.e., natural sunlight or artificial light) and the scene type (i.e., indoor or outdoor scene).
- The third category of influencing factors addresses characteristics of the observed scene in terms of object materials, surface reflectivity, and surface roughness which strongly influence light reflection on the object surfaces [27, 48, 57].
- The fourth category of influencing factors addresses the scanning geometry [2, 35], i.e., the distance and orientation of scanned surfaces with respect to the involved sensor. Particularly the incidence angle representing the angle between incoming laser beam and surface normal strongly influences individual point quality [42, 43], but also those effects occurring at object edges have to be addressed [4].

While a systematic error modeling may account for potential error sources arising from the acquisition system [3, 8, 28, 29], scene-specific issues cannot be generalized and therefore have to be treated differently. In the scope of our work, we focus on terrestrial laser scanning and mobile laser scanning in outdoor environments with reasonable natural sunlight. Consequently, we face relatively small distances between scene objects and the acquisition system as well as relatively small displacements of the acquisition system for obtaining consecutive scans, so that atmospheric and environmental conditions may be neglected. Furthermore, we do not make assumptions on the presence of specific object materials and the corresponding surface reflectivity, since we focus on digitizing arbitrary scenes without involving prior knowledge about the presence and the surface reflectance behavior of specific materials. As a consequence, we mainly focus on the scanning geometry and the reflected energy (represented as intensity value) per range measurement. Thus, we may treat the quantification of the quality of a range measurement decoupled in a post-processing step.

The decoupled consideration may also directly be applied for available benchmark datasets, where we may purely focus on filtering available raw 3D point cloud data by exploiting the captured information. On the one hand, a simple approach for removing unreliable range measurements may be based on the captured intensity information [4], since very low intensity values are likely to correspond to unreliable range measurements. On the other hand, it seems desirable to explicitly address points at depth discontinuities as these exhibit the largest uncertainty in distance. A respective filtering may, for instance, be achieved by considering the variance of the local normal vector [2], by removing 3D points corresponding to nonplanar objects or objects which are susceptible to occlusions, shadows, etc. [16, 17], by applying the Laplacian operator on the range image [5] or by involving the scan line approximation technique [14]. Accounting for both intensity and range information, the combination of removing points with low values in the intensity image as well as points at edges in the range image has been proposed in order to obtain an adequate 3D representation of a scene [45]. Furthermore, it should be taken into account that the scanning geometry with respect to the incidence angle may have a significant influence on the accuracy of a range measurement which becomes visible by an increase in measurement noise with increasing incidence angles [43]. Accordingly, it would be desirable to have a common and generic measure which considers reliability in terms of both object edges and incidence angle.

### *2.5.2 Filtering Based on Intensity Information*

As already mentioned above, a filtering of raw 3D point cloud data may be based on intensity information [4], since low intensity values typically indicate unreliable range measurements. Consequently, the main challenge of such an approach consists of finding a suitable threshold in order to distinguish reliable range measurements from unreliable ones. Such a threshold may for instance be derived by applying

a histogram-based approach estimating a suitable border between bimodal distributions. However, the measured intensity values may be arbitrary and significantly vary from one device to another, since they depend on the electronic circuits inside the scanning device. A transfer toward a general application across a variety of different scanning devices may easily be derived by applying a histogram normalization and thereby mapping the measured intensity values onto a predefined fixed interval whose borders may principally be selected arbitrarily. Accordingly, we may for instance select the interval [0, 1], but—as we have already derived a 2D image representation of intensity information in the form of an 8-bit gray-valued image (Sect. 2.4)—it is feasible to use the interval [0, 255] instead and select the threshold as a specific gray value $t_{\mathrm{I,gray}}$. Note that such a simple thresholding based on intensity information may also be used to detect and remove soft obstacles which are for instance given by smoke, dust, fog or steam [11].

While an intensity-based filtering of raw 3D point cloud data is straightforward, easy-to-implement, and quite efficient,[5] such considerations do not account for edge effects where noisy range measurements are likely to occur although the respective intensity values might be reasonable. Hence, we focus on two novel strategies which are based on the geometric measures of (i) *range reliability* and (ii) *local planarity* in order to quantify the quality of a range measurement.

### 2.5.3 Filtering Based on Range Reliability

The first of our proposed measures to quantify the reliability of a range measurement directly addresses the fact that—instead of considering a laser beam as a ray with no physical dimensions—it is inevitable that a laser beam has certain physical dimensions which, in turn, influences the laser beam propagation. Thus, the projection of a laser beam on the target area results in a *laser footprint*, i.e., a spot with finite dimension, that may vary depending on the slope of the local surface and material characteristics [50]. Consequently, if a measured 3D point corresponds to a laser footprint on a geometrically smooth surface, the captured range information is rather reliable when assuming Lambertian surfaces and reasonable incidence angles. However, at edges of objects, a laser footprint may cover surfaces at different distances to the sensor, and thus the captured range information is rather unreliable. Even more critical are range measurements corresponding to the sky, since these mainly arise from atmospheric effects.

In order to quantify these effects and remove unreliable range measurements—which would typically appear as noisy behavior in a visualization of the considered 3D point cloud data—our first measure referred to as *range reliability* [51] is based on the categorization of each point on the 2D scan grid by considering local image

[5] For our image-based consideration, we only need to calculate the sign-function of the difference of the intensity image $\mathscr{I}_{\mathrm{I}}$ and an image $\mathscr{I}_{\mathrm{I}}^{*} = t_{\mathrm{I,gray}} \cdot \mathbf{1}_{n \times m} \in \mathbb{R}^{n \times m}$ of constant gray value $t_{\mathrm{I,gray}}$, which yields pixel-wise conclusions about reliable or unreliable range measurements.

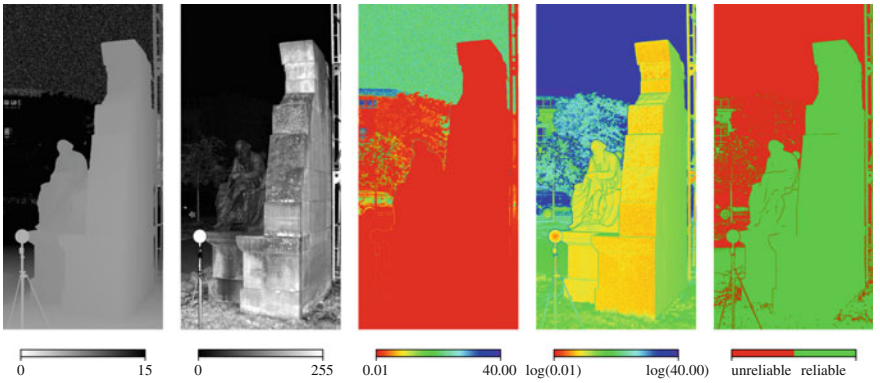


**Fig. 2.4** Range image $\mathscr{I}_{\mathrm{R}}$, intensity image $\mathscr{I}_{\mathrm{I}}$, visualization of range reliability $\sigma_{r,3\times3}$, logarithmic representation of range reliability $\sigma_{r,3\times3}$ and the binary confidence map derived by thresholding based on a manually selected threshold of $t_\sigma = 0.03\,\mathrm{m}$ (from *left* to *right*)

patches in the respective range image. More specifically, this measure considers a local $(3 \times 3)$ image neighborhood for each pixel $(x, y)$ in the range image and assigns the standard deviation $\sigma_{r,3\times3}$ of all range values $r$ within the $(3 \times 3)$ image neighborhood to $(x, y)$. Deriving $\sigma_{r,3\times3}$ for all pixels of the range image yields a confidence map. In this confidence map, low values $\sigma_{r,3\times3}$ indicate a 3D point on a smooth surface and are therefore assumed to correspond to reliable range measurements, whereas high values $\sigma_{r,3\times3}$ indicate noisy and unreliable range measurements. Consequently, a simple thresholding based on a predefined threshold $t_\sigma$ may be considered as sufficient to separate reliable measurements from unreliable ones in a binary confidence map, which is shown in Fig. 2.4 for a part of a terrestrial laser scan which corresponds to $2304 \times 1135$ scanned 3D points and has been acquired with a Leica HDS6000 on the KIT campus in Karlsruhe, Germany. According to qualitative tests involving different scanning devices, a value of $t_\sigma = 0.03 \ldots 0.10\,\mathrm{m}$ has proven to be appropriate for data captured with a terrestrial laser scanner [51] and for data captured with a range camera [54, 55], but the manual selection of a threshold based on prior knowledge about the scene and/or data represents a limitation.

### *2.5.4 Filtering Based on Local Planarity*

The second of our proposed measures which we refer to as *local planarity* [52] is motivated by the fact that reliable range information typically corresponds to almost planar structures in the scene which are characterized by low incidence angles. Consequently, we aim to quantify the local planarity for each point on the 2D scan grid by considering local image patches in the respective range image. In analogy to the measure of range reliability, we consider $(3 \times 3)$ image neighborhoods as local

image patches in order to assign a measure of planarity to the respective center point. From the spatial *XYZ*-coordinates of all 3D points corresponding to the pixels in the $(3 \times 3)$ image neighborhood, we derive the 3D covariance matrix known as *3D structure tensor* $\mathbf{S}_{3D} \in \mathbb{R}^{3\times3}$ whose eigenvalues $\lambda_1, \lambda_2, \lambda_3 \in \mathbb{R}$ with $\lambda_1 \geq \lambda_2 \geq \lambda_3 \geq 0$ are further exploited in order to define the *dimensionality features* of *linearity* $L_\lambda$, *planarity* $P_\lambda$ and *scattering* $S_\lambda$ [58]:

$$L_\lambda = \frac{\lambda_1 - \lambda_2}{\lambda_1} \qquad P_\lambda = \frac{\lambda_2 - \lambda_3}{\lambda_1} \qquad S_\lambda = \frac{\lambda_3}{\lambda_1} \tag{2.2}$$

These dimensionality features reveal a normalization by the largest eigenvalue $\lambda_1$, so that they sum up to 1 and the largest value among the dimensionality features indicates the characteristic behavior of the respective pixel. Accordingly, a pixel $(x, y)$ in the range image represents a planar 3D structure and therefore rather reliable range information if the local planarity $P_{\lambda,3\times3}$ in a $(3 \times 3)$ image neighborhood satisfies the constraint

$$P_{\lambda,3\times3} := P_\lambda \geq \max\{L_\lambda, S_\lambda\} \tag{2.3}$$

which—in contrast to the measure of range reliability—yields a binary confidence map (e.g., as illustrated in Fig. 2.5) in a fully generic manner without involving any manually specified thresholds and thus prior knowledge about the scene and/or data.

Note that the dimensionality features could also directly be extracted for each point of the 3D point cloud by considering other 3D points in the local 3D neighborhood and exploiting the respective 3D structure tensor in order to derive the eigenvalues. However, particularly for large point clouds, it can be quite time-consuming to extract suitable neighborhoods and, in turn, the dimensionality features resulting from the eigenvalues of the 3D structure tensor. Consequently, the proposed consideration of

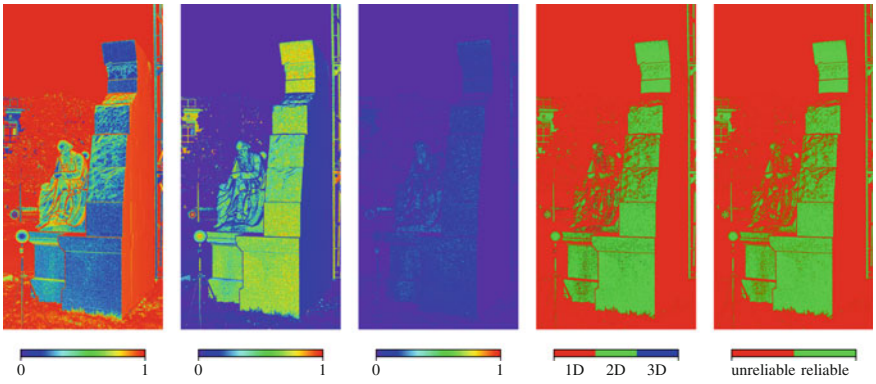


**Fig. 2.5** Visualization of linearity $L_\lambda$, planarity $P_\lambda$, scattering $S_\lambda$, the classification of each pixel according to its local behavior (linear (1D): *red*; planar (2D): *green*; scattered (3D): *blue*) and the derived binary confidence map (from *left* to *right*)

local planarity $P_{\lambda,3\times3}$ based on a local $(3 \times 3)$ image neighborhood offers the great advantage that the direct neighbors of each point on the regular 2D scan grid may be derived more efficiently with respect to processing time and memory consumption than a suitable number of neighbors in 3D.

### 2.5.5 *A Qualitative Comparison of Different Measures*

In order to provide an impression about the performance of the different measures for quantifying the quality of range measurements, we consider 2D image representations for range and intensity information in Fig. 2.6 as well as the respective binary confidence maps based on (i) intensity information when applying a threshold of $t_{\mathrm{I,gray}} = 10$ (for an 8-bit gray-valued image), (ii) the measure $\sigma_{r,3\times3}$ of range reliability when applying a threshold of $t_\sigma = 0.03\,\mathrm{m}$, and (iii) the generic measure $P_{\lambda,3\times3}$ of local planarity. For each measure, the corresponding effect in 3D space is visualized in Fig. 2.7. This figure clearly reveals that the use of intensity information alone is not sufficient to adequately filter raw 3D point cloud data and thereby completely remove the noisy behavior. In contrast, the strategies based on the two geometric measures retain adequate representations of local object surfaces. Whereas the strategy based on the measure $\sigma_{r,3\times3}$ of range reliability provides almost planar object surfaces for significantly varying incidence angles (Fig. 2.6), the strategy based on the measure $P_{\lambda,3\times3}$ of local planarity only provides almost perpendicular object surfaces with almost planar behavior and thus favors lower incidence angles which tend to yield more accurate range measurements. Note that, even though the sphere target in the lower left part of the depicted images does not provide a planar surface, the measures of range reliability and local planarity indicate reliable range measurements for almost all points corresponding to the surface of the sphere target, and only points

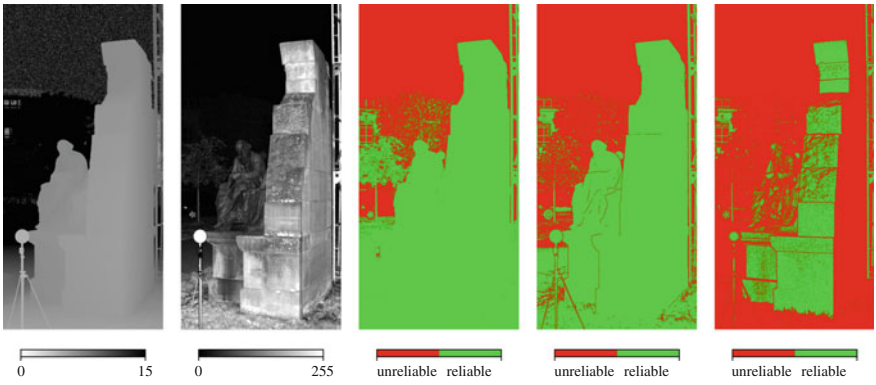


**Fig. 2.6** Range image $\mathscr{I}_\mathrm{R}$, intensity image $\mathscr{I}_\mathrm{I}$, and the derived binary confidence maps based on intensity information, range reliability $\sigma_{r,3\times3}$ and local planarity $P_{\lambda,3\times3}$ (from *left* to *right*)

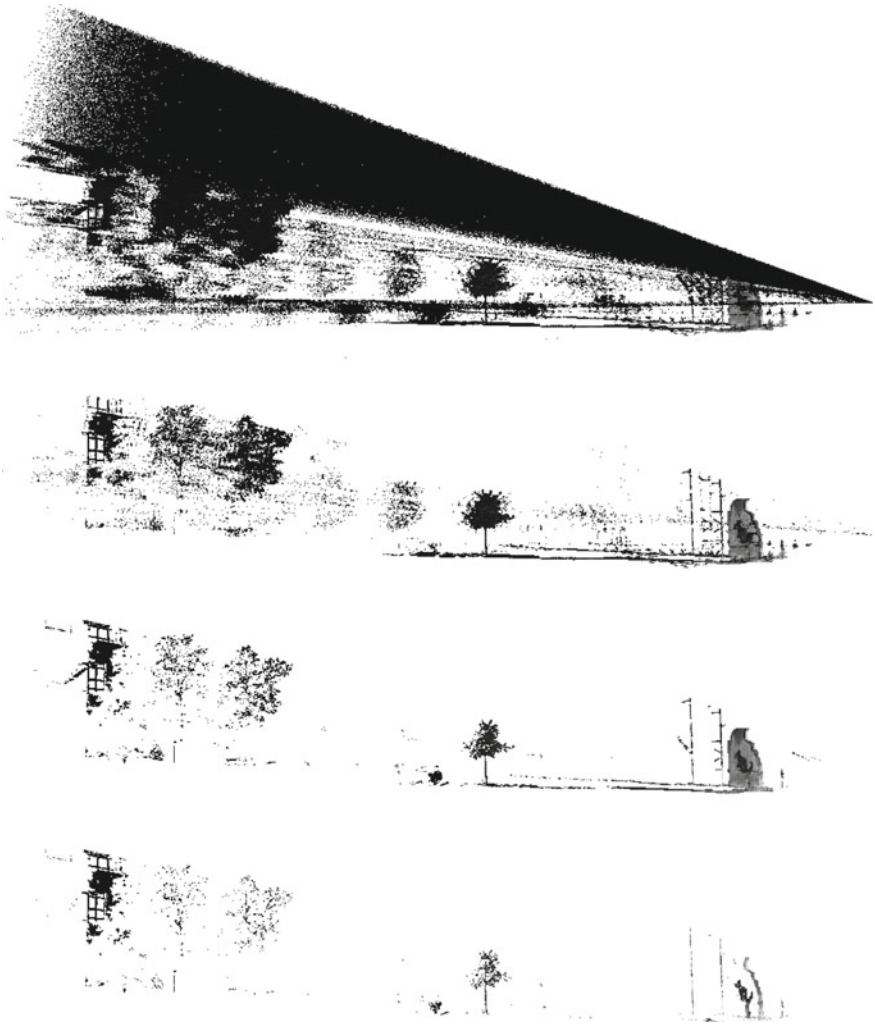

**Fig. 2.7** Raw 3D point cloud data, 3D point cloud data filtered via intensity information, 3D point cloud data filtered via the measure $\sigma_{r,3\times3}$ of range reliability and 3D point cloud data filtered via the measure $P_{\lambda,3\times3}$ of local planarity (from *top* to *bottom*)

at the edges are considered as unreliable. This is due to the consideration of relatively small ($3 \times 3$) image neighborhoods, where no significant deviation in range direction and no significant deviation from a locally planar surface may be observed.

### 2.5.6 A Quantitative Comparison of Different Measures

In this section, we intend to quantitatively compare the different measures for point quality assessment and verify our observations made in the previous subsection. For this purpose, we consider a fairly simple scenario and carry out theoretical considerations for the proposed measures of range reliability $\sigma_{r,3\times3}$ and local planarity $P_{\lambda,3\times3}$ and, thereby, we aim to point out consequences concerning what we may expect when applying these measures on range images. This is of utmost importance since we may thus easily explain the significant differences between the binary confidence maps depicted in Figs. 2.4 and 2.5.

The considered scenario focuses on the characteristics of scanned 3D points on a planar surface with a certain distance and a certain incidence angle with respect to the scanning device. Considering fundamentals of projective geometry as for instance described in [15], the 3D coordinates of any point $\mathbf{X} \in \mathbb{R}^3$ on a ray in 3D space satisfy the constraint $\mathbf{X} = \mathbf{A} + b\mathbf{v}$, where $\mathbf{A} \in \mathbb{R}^3$ denotes a known 3D point on the ray, $b \in \mathbb{R}$ represents a scalar factor and $\mathbf{v} \in \mathbb{R}^3$ indicates the direction of the ray. Without loss of generality, we may transfer this equation from world coordinates to camera coordinates as indicated by a superscript $^c$, i.e., $\mathbf{X}^c = \mathbf{A}^c + b\mathbf{v}^c$. Note that assuming the model of a pinhole camera is valid when using range cameras and approximately valid when considering a local $(3 \times 3)$ neighborhood on a spherical scan grid with reasonable angular resolution. Since the considered rays thus intersect each other at the projective center $\mathbf{0}^c$, it is straightforward to use the point $\mathbf{A}^c = \mathbf{0}^c = [0, 0, 0]^T$ as known 3D point on all rays. Following the standard definitions, we may furthermore define the camera coordinate frame relative to the device in a way so that the $X^c$-axis points to the right, the $Y^c$-axis to the bottom and the $Z^c$-axis in depth. Considering a local $(3 \times 3)$ image neighborhood, we may conduct point quality assessment by looking along the $Z^c$-axis and assuming an angular resolution $\Delta\alpha$ of the camera. Accordingly, the directions $\mathbf{v}^c$ of the 8 neighboring rays which are exploited to obtain a local $(3 \times 3)$ image neighborhood may easily be derived by an intersection with the $(Z^c = 1)$-plane and we thus evaluate the geometric behavior of range measurements in a field-of-view given by $(2\Delta\alpha \times 2\Delta\alpha)$. Note that, in this context, typical angular resolutions would be $\Delta\alpha \approx \{0.36°$ (middle scan density), $0.18°$ (high scan density), $0.09°$ (super high scan density), $0.05°$ (ultra high scan density)$\}$ for a terrestrial laser scanner of type Leica HDS6000, $\Delta\alpha \approx 0.2°$ for a range camera of type PMD[vision] CamCube 2.0 and $\Delta\alpha \approx 0.09°$ for a range camera of type Microsoft Kinect.

Once the rays have been derived for a field-of-view of $(2\Delta\alpha \times 2\Delta\alpha)$, we may proceed by assuming that these rays intersect a plane $\boldsymbol{\pi}$ which is parameterized in the camera coordinate frame by a 3D point $\mathbf{X}_{\boldsymbol{\pi}}^c$ and a normal vector $\mathbf{n}_{\boldsymbol{\pi}}^c \in \mathbb{R}^3$. Thereby, we define the 3D point $\mathbf{X}_{\boldsymbol{\pi}}^c$ as the point which results from the intersection of $\boldsymbol{\pi}$ with the $Z^c$-axis, and we further assume that the distance between $\mathbf{X}_{\boldsymbol{\pi}}^c$ and $\mathbf{0}^c$ is given by $d$, i.e., $\mathbf{X}_{\boldsymbol{\pi}}^c = [0, 0, d]^T$. Initially, we consider the case of a normal vector $\mathbf{n}_{\boldsymbol{\pi}}^c$ which coincides with the $Z^c$-axis, and thus the plane $\boldsymbol{\pi}$ is perpendicular to the $Z^c$-axis and parallel to the $X^cY^c$-plane. Subsequently, we rotate the plane $\boldsymbol{\pi}$ by an angle $\beta$ around the axis defined by the point $\mathbf{X}_{\boldsymbol{\pi}}^c = [0, 0, d]^T$ and the direction $[0, 1, 0]^T$ in

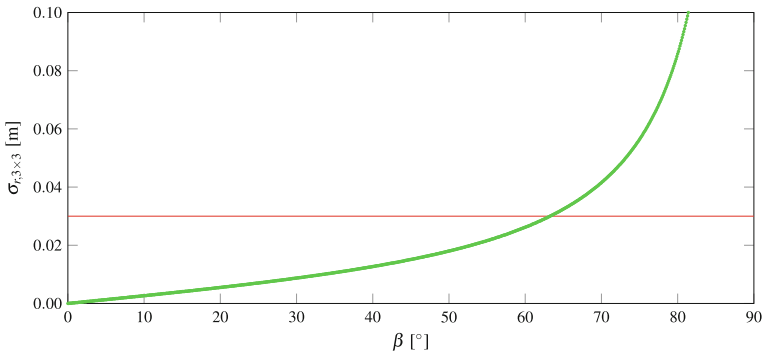


**Fig. 2.8** Behavior of the measure $\sigma_{r,3\times3}$ of range reliability for increasing incidence angles $\beta$. The applied threshold of $t_\sigma = 0.03\,\text{m}$ is indicated with a *red line*

the camera coordinate frame. As a result, the angle $\beta$ coincides with the incidence angle and we get 9 points of intersection for angles $\beta \in [0°, 90°)$.

In order to verify the suitability of the proposed measure $\sigma_{r,3\times3}$ of range reliability, we simply exploit the distances between the projective center $\mathbf{0}^c$ and the 9 points of intersection. These distances correspond to range measurements and the measure $\sigma_{r,3\times3}$ of range reliability (see Sect. 2.5.3) simply represents the standard deviation of the 9 considered distances (i.e., range values). For a representative example, we consider the use of a range camera of type PMD[vision] CamCube 2.0 and, accordingly, we select the angular resolution to $\Delta\alpha = 0.2°$ and the distance between projective center $\mathbf{0}^c$ and $\mathbf{X}_{\pi}^c$ to $d = 5\,\text{m}$. The respective behavior of $\sigma_{r,3\times3}$ for varying incidence angles is visualized in Fig. 2.8. This figure clearly reveals that, when applying the proposed threshold of $t_\sigma = 0.03\,\text{m}$, range measurements are assumed to be reliable for incidence angles of less than about 63.3°. A less strict threshold of $t_\sigma = 0.10\,\text{m}$ even results in reliable range measurements up to incidence angles of about 81.4°.

In order to verify the suitability of the proposed measure $P_{\lambda,3\times3}$ of local planarity, we exploit the 3D coordinates of the 9 points of intersection in order to derive the 3D structure tensor $\mathbf{S}_{3D}$ and its eigenvalues $\lambda_1$, $\lambda_2$ and $\lambda_3$ as well as the dimensionality features of linearity $L_\lambda$, planarity $P_\lambda$ and scattering $S_\lambda$ (see Sect. 2.5.4). For a representative example, we again consider the use of a range camera of type PMD[vision] CamCube 2.0 and, accordingly, we select the angular resolution to $\Delta\alpha = 0.2°$ and the distance between projective center $\mathbf{0}^c$ and $\mathbf{X}_{\pi}^c$ to $d = 5\,\text{m}$. The respective values of the dimensionality features for angles $\beta \in [0°, 90°)$ are depicted in Fig. 2.9, and they reveal that the locally planar 3D structure provides a planar behavior in the interval $[0°, 45°]$ and a linear behavior beyond this interval. As a consequence, range measurements are assumed to be reliable if the local $(3 \times 3)$ image neighborhood represents a locally planar 3D structure with an incidence angle in $[0°, 45°]$. Note that, due to the narrow field-of-view of $(2\Delta\alpha \times 2\Delta\alpha)$ for a local $(3 \times 3)$ image patch, noisy range measurements e.g., corresponding to the sky will not be indicated by a scattered behavior, but by a linear behavior since only a significant variation in ray

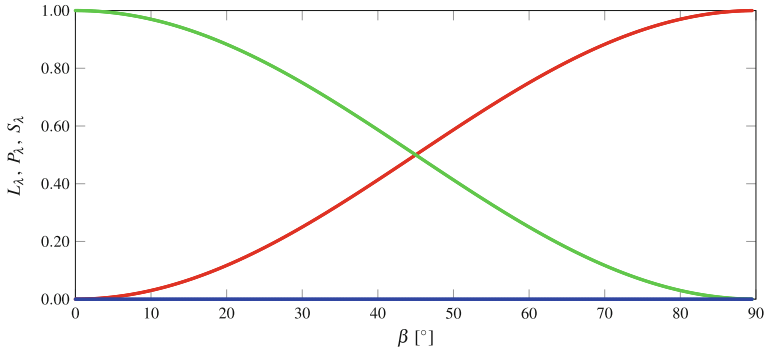


**Fig. 2.9** Behavior of the dimensionality features of linearity $L_\lambda$ (*red*), planarity $P_\lambda$ (*green*), and scattering $S_\lambda$ (*blue*) for increasing incidence angles $\beta$

direction will be present. Furthermore considering that the dimensionality features are normalized by the largest eigenvalue, our observations on reliable range measurements in terms of local planarity are independent from both the angular resolution $\Delta\alpha$ and the distance between $\mathbf{X}_\pi^c$ and $\mathbf{0}^c$.

Based on these results, the considered scenario allows to provide qualitative statements on the suitability of both measures. The binary confidence map shown in Fig. 2.4 provides more reliable range measurements than the binary confidence map depicted in Fig. 2.5, particularly for those scanned 3D points on planar surfaces with a higher incidence angle. The reason for this behavior becomes visible when comparing Figs. 2.8 and 2.9, since applying the measure $\sigma_{r,3\times3}$ of range reliability also allows incidence angles which are much larger than 45°, whereas the measure $P_{\lambda,3\times3}$ of local planarity relates reliable range measurements to planar surfaces with incidence angles of up to only about 45°. Furthermore, it should be taken into account that, while the measure $\sigma_{r,3\times3}$ of range reliability depends on the distances between the projective center and the 9 points of intersection as well as the angular resolution $\Delta\alpha$ of the scanning device, the measure $P_{\lambda,3\times3}$ of local planarity is independent from both of them.

## 2.6 Conclusions

In this chapter, we have described fundamentals concerning the definition of 3D point clouds and their acquisition. Focusing on active point cloud acquisition via laser scanners and range cameras, we have addressed the issue of how to transform the captured 3D point cloud data to 2D representations in the form of range images and intensity images, since such images allow to exploit a rich variety of approaches which have proven to be effective and efficient for tasks such as feature extraction, object recognition, or object segmentation. Furthermore, we have provided an

overview on techniques for judging about the quality of each 3D point by considering the reliability of the respective range measurement and, in this context, we have presented two novel approaches and discussed their capabilities. From a comparison of 3D visualizations of raw 3D point cloud data and, respectively, filtered 3D point cloud data for an exemplary TLS scan, we may conclude that a filtering based on point quality assessment might not only visually improve the results, but also alleviate subsequent tasks relying on either all or only some of the acquired 3D points. Later, in Chap. 4, we will make use of the presented concepts for (i) generating 2D representations and (ii) assessing point quality in the context of point cloud registration, and we will see significant advantages arising from such concepts.

## References

1. Agarwal S, Snavely N, Simon I, Seitz SM, Szeliski R (2009) Building Rome in a day. In: Proceedings of the IEEE international conference on computer vision, pp 72–79
2. Bae K-H, Belton D, Lichti DD (2005) A framework for position uncertainty of unorganised three-dimensional point clouds from near-monostatic laser scanners using covariance analysis. Int Arch Photogramm Remote Sens Spat Inf Sci XXXVI-3/W19:7–12
3. Barber D, Mills J, Smith-Voysey S (2008) Geometric validation of a ground-based mobile laser scanning system. ISPRS J Photogramm Remote Sens 63(1):128–141
4. Barnea S, Filin S (2007) Registration of terrestrial laser scans via image based features. Int Arch Photogramm Remote Sens Spat Inf Sci XXXVI-3/W52:32–37
5. Barnea S, Filin S (2008) Keypoint based autonomous registration of terrestrial laser point-clouds. ISPRS J Photogramm Remote Sens 63(1):19–35
6. Boehler W, Bordas Vicent M, Marbs A (2003) Investigating laser scanner accuracy. Int Arch Photogramm Remote Sens Spat Inf Sci XXXIV-5/C15:1–6
7. Borah DK, Voelz DG (2007) Estimation of laser beam pointing parameters in the presence of atmospheric turbulence. Appl Opt 46(23):6010–6018
8. Boström G, Gonçalves JGM, Sequeira V (2008) Controlled 3D data fusion using error-bounds. ISPRS J Photogramm Remote Sens 63(1):55–67
9. Brenner C, Dold C, Ripperda N (2008) Coarse orientation of terrestrial laser scans in urban environments. ISPRS J Photogramm Remote Sens 63(1):4–18
10. Dal Mutto C, Zanuttigh P, Cortelazzo GM (2012) Time-of-flight cameras and Microsoft Kinect(TM). Springer, New York
11. Djuricic A, Jutzi B (2013) Supporting UAVs in low visibility conditions by multiple-pulse laser scanning devices. Int Arch Photogramm Remote Sens Spat Inf Sci XL-1/W1:93–98
12. Droeschel D, Holz D, Behnke S (2010) Multi-frequency phase unwrapping for time-of-flight cameras. In: Proceedings of the IEEE/RSJ international conference on intelligent robots and systems, pp 1463–1469
13. Frahm J-M, Fite-Georgel P, Gallup D, Johnson T, Raguram R, Wu C, Jen Y-H, Dunn E, Clipp B, Lazebnik S, Pollefeys M (2010) Building Rome on a cloudless day. In: Proceedings of the European conference on computer vision, vol IV, pp 368–381
14. Fuchs S, May S (2008) Calibration and registration for precise surface reconstruction with time-of-flight cameras. Int J Intell Syst Technol Appl 5(3/4):274–284
15. Hartley RI, Zisserman A (2008) Multiple view geometry in computer vision. University Press, Cambridge
16. Hebel M, Stilla U (2007) Automatic registration of laser point clouds of urban areas. Int Arch Photogramm Remote Sens Spat Inf Sci XXXVI-3/W49A:13–18

17. Hebel M, Stilla U (2009) Automatische Koregistrierung von ALS-Daten aus mehreren Schrägansichten städtischer Quartiere. PFG—Photogramm Fernerkund Geoinf 3(2009):261–275
18. Hebert M, Krotkov E (1992) 3-D measurements from imaging laser radars: how good are they? Int J Image Vis Comput 10(3):170–178
19. Hennes M (2007) Konkurrierende Genauigkeitsmaße—Potential und Schwächen aus der Sicht des Anwenders. AVN—Allg Vermess-Nachr 4(2007):136–146
20. Herbort S, Wöhler C (2011) An introduction to image-based 3D surface reconstruction and a survey of photometric stereo methods. 3D Res 2(3):40:1–40:17
21. Jutzi B (2007) Analyse der zeitlichen Signalform von rückgestreuten Laserpulsen. PhD thesis, Institut für Photogrammetrie und Kartographie, Technische Universität München, München, Germany
22. Jutzi B (2009) Investigations on ambiguity unwrapping of range images. Int Arch Photogramm Remote Sens Spat Inf Sci XXXVIII-3/W8:265–270
23. Jutzi B (2012) Extending the range measurement capabilities of modulated range imaging devices by time-frequency-multiplexing. AVN—Allg Vermess-Nachr 2(2012):54–62
24. Jutzi B (2015) Methoden zur automatischen Szenencharakterisierung basierend auf aktiven optischen Sensoren für die Photogrammetrie und Fernerkundung. Habilitation thesis, Institute of Photogrammetry and Remote Sensing, Karlsruhe Institute of Technology (KIT), Karlsruhe, Germany
25. Khoshelham K, Oude Elberink S (2012) Accuracy and resolution of Kinect depth data for indoor mapping applications. Sensors 12(2):1437–1454
26. Kolb A, Barth E, Koch R, Larsen R (2010) Time-of-flight cameras in computer graphics. Comput Graph Forum 29(1):141–159
27. Leader JC (1979) Analysis and prediction of laser scattering from rough-surface materials. J Opt Soc Am A 69(4):610–628
28. Lichti DD, Gordon SJ, Tipdecho T (2005) Error models and propagation in directly georeferenced terrestrial laser scanner networks. J Survey Eng 131(4):135–142
29. Lichti DD, Licht MG (2006) Experiences with terrestrial laser scanner modelling and accuracy assessment. Int Arch Photogramm Remote Sens Spat Inf Sci XXXVI-5:155–160
30. Moons T, Van Gool L, Vergauwen M (2010) 3D reconstruction from multiple images—Part 1: principles. Found Trends Comput Graph Vis 4(4):287–404
31. Remondino F, Stoppa D (2013) TOF range-imaging cameras. Springer, Heidelberg
32. Rusu RB, Cousins S (2011) 3D is here: Point Cloud Library (PCL). In: Proceedings of the IEEE international conference on robotics and automation, pp 1–4
33. Salvi J, Pagès J, Batlle J (2004) Pattern codification strategies in structured light systems. Pattern Recognit 37(4):827–849
34. Sansoni G, Trebeschi M, Docchio F (2009) State-of-the-art and applications of 3D imaging sensors in industry, cultural heritage, medicine, and criminal investigation. Sensors 9(1):568–601
35. Schaer P, Legat K, Landtwing S, Skaloud J (2007) Accuracy estimation for laser point cloud including scanning geometry. Int Arch Photogramm Remote Sens Spat Inf Sci XXXVI-5/C55:1–8
36. Scharstein D, Szeliski R (2002) A taxonomy and evaluation of dense two-frame stereo correspondence algorithms. Int J Comput Vis 47(1–3):7–42
37. Seitz SM, Curless B, Diebel J, Scharstein D, Szeliski R (2006) A comparison and evaluation of multi-view stereo reconstruction algorithms. In: Proceedings of the IEEE computer society conference on computer vision and pattern recognition, vol 1, pp 519–528
38. Smisek J, Jancosek M, Pajdla T (2011) 3D with Kinect. In: Proceedings of the IEEE international conference on computer vision workshops, pp 1154–1160
39. Soatto S (2009) Actionable information in vision. In: Proceedings of the IEEE international conference on computer vision, pp 2138–2145
40. Soatto S (2011) Steps towards a theory of visual information: active perception, signal-to-symbol conversion and the interplay between sensing and control. Technical Report, arXiv:1110.2053 [cs.CV]

41. Soudarissanane S, Lindenbergh R (2011) Optimizing terrestrial laser scanning measurement set-up. Int Arch Photogramm Remote Sens Spat Inf Sci XXXVIII-5/W12:127–132
42. Soudarissanane S, Lindenbergh R, Menenti M, Teunissen P (2009) Incidence angle influence on the quality of terrestrial laser scanning points. Int Arch Photogramm Remote Sens Spat Inf Sci XXXVIII-3/W8:183–188
43. Soudarissanane S, Lindenbergh R, Menenti M, Teunissen P (2011) Scanning geometry: influencing factor on the quality of terrestrial laser scanning points. ISPRS J Photogramm Remote Sens 66(4):389–399
44. Stilla U, Jutzi B (2009) Waveform analysis for small-footprint pulsed laser systems. In: Shan J, Toth CK (eds) Topographic laser ranging and scanning: principles and processing. CRC Press, Boca Raton, pp 215–234
45. Swadzba A, Liu B, Penne J, Jesorsky O, Kompe R (2007) A comprehensive system for 3D modeling from range images acquired from a 3D ToF sensor. In: Proceedings of the international conference on computer vision systems, pp 1–10
46. Szeliski R (2011) Computer vision: algorithms and applications. Springer, London
47. Triggs B, McLauchlan PF, Hartley RI, Fitzgibbon AW (1999) Bundle adjustment—A modern synthesis. In: Proceedings of the international workshop on vision algorithms: theory and practice, pp 298–372
48. Voegtle T, Schwab I, Landes T (2008) Influences of different materials on the measurements of a terrestrial laser scanner (TLS). Int Arch Photogramm Remote Sens Spat Inf Sci XXXVII-B5:1061–1066
49. Voisin S, Foufou S, Truchetet F, Page D, Abidi M (2007) Study of ambient light influence for three-dimensional scanners based on structured light. Opt Eng 46(3):030502:1–3
50. Vosselman G, Maas H-G (2010) Airborne and terrestrial laser scanning. Whittles Publishing, Dunbeath
51. Weinmann M, Jutzi B (2011) Fully automatic image-based registration of unorganized TLS data. Int Arch Photogramm Remote Sens Spat Inf Sci XXXVIII-5/W12:55–60
52. Weinmann M, Jutzi B (2015) Geometric point quality assessment for the automated, markerless and robust registration of unordered TLS point clouds. ISPRS Ann Photogramm Remote Sens Spat Inf Sci II-3/W5:89–96
53. Weinmann M, Wursthorn S, Jutzi B (2011) Semi-automatic image-based fusion of range imaging data with different characteristics. Int Arch Photogramm Remote Sens Spat Inf Sci XXXVIII-3/W22:119–124
54. Weinmann M, Dittrich A, Hinz S, Jutzi B (2013) Automatic feature-based point cloud registration for a moving sensor platform. Int Arch Photogramm Remote Sens Spat Inf Sci XL-1/W1:373–378
55. Weinmann M, Leitloff J, Hoegner L, Jutzi B, Stilla U, Hinz S (2014) Thermal 3D mapping for object detection in dynamic scenes. ISPRS Ann Photogramm Remote Sens Spat Inf Sci II-1:53–60
56. Weinmann Mi, Osep A, Ruiters R, Klein R (2013) Multi-view normal field integration for 3D reconstruction of mirroring objects. In: Proceedings of the IEEE international conference on computer vision, pp 2504–2511
57. Weinmann Mi, Klein R (2015) Advances in geometry and reflectance acquisition (course notes). In: Proceedings of the SIGGRAPH Asia 2015 Courses, pp 1:1–1:71
58. West KF, Webb BN, Lersch JR, Pothier S, Triscari JM, Iverson AE (2004) Context-driven automated target detection in 3-D data. Proc SPIE 5426:133–143
59. Wursthorn S (2014) Kamerabasierte Egomotion-Bestimmung mit natürlichen Merkmalen zur Unterstützung von Augmented-Reality-Systemen. PhD thesis, Institute of Photogrammetry and Remote Sensing, Karlsruhe Institute of Technology (KIT), Karlsruhe, Germany

http://www.springer.com/978-3-319-29244-1

Reconstruction and Analysis of 3D Scenes
From Irregularly Distributed 3D Points to Object Classes
Weinmann, M.
2016, XXII, 233 p. 81 illus., 69 illus. in color., Hardcover
ISBN: 978-3-319-29244-1